

Integrating RNA expression and visual features for immune infiltrate prediction

Derek Reiman¹, Lingdao Sha¹, Irvin Ho¹, Timothy Tan², Denise Lau^{1,†}, and Aly A. Khan^{1,3,†}

¹*Tempus Labs, Chicago, IL 60654, USA*, ²*Department of Pathology, Northwestern University, Chicago, IL 60637, USA*, ³*Toyota Technological Institute at Chicago, Chicago, IL 60611, USA*.

[†]*Corresponding authors: denise@tempus.com; aakhan@ttic.edu*

Patient responses to cancer immunotherapy are shaped by their unique genomic landscape and tumor microenvironment. Clinical advances in immunotherapy are changing the treatment landscape by enhancing a patient's immune response to eliminate cancer cells. While this provides potentially beneficial treatment options for many patients, only a minority of these patients respond to immunotherapy. In this work, we examined RNA-seq data and digital pathology images from individual patient tumors to more accurately characterize the tumor-immune microenvironment. Several studies implicate an inflamed microenvironment and increased percentage of tumor infiltrating immune cells with better response to specific immunotherapies in certain cancer types. We developed NEXT (Neural-based models for integrating gene EXpression and visual Texture features) to more accurately model immune infiltration in solid tumors. To demonstrate the utility of the NEXT framework, we predicted immune infiltrates across four different cancer types and evaluated our predictions against expert pathology review. Our analyses demonstrate that integration of imaging features improves prediction of the immune infiltrate. Of note, this effect was preferentially observed for B cells and CD8 T cells. In sum, our work effectively integrates both RNA-seq and imaging data in a clinical setting and provides a more reliable and accurate prediction of the immune composition in individual patient tumors.

Keywords: Cancer immunology, digital pathology, immune infiltration, machine learning.

1. Introduction

Immune infiltration and its spatial organization within the tumor microenvironment has long been associated with cancer progression and clinical outcome.^{1,2} The potential of the immune infiltrate as a prognostic biomarker has become increasingly relevant with the advent of cancer immunotherapies. Checkpoint blockade and other cancer immunotherapies can induce clinical responses in some cancer patients.^{3,4} However, clinical responses are only observed in a proportion of patients and vary for different cancer types, suggesting that additional factors, such as the composition of the immune infiltrate, may be important determinants of clinical response.^{5,6} Several clinical studies show the tumor immune microenvironment, particularly the presence or absence of key effector cells such as CD8 T cells, can affect tumor immune responses.^{7,8} The challenge, then, is to develop accurate methods to characterize the immune infiltrate in cancer patients in a reproducible and cost effective manner in order to ultimately identify novel prognostic markers.

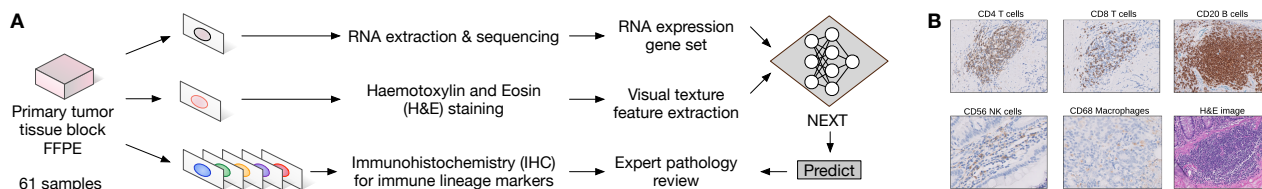


Fig. 1. Multi-modal approach used to train and validate NEXt for predicting the tumor immune infiltrate fraction and composition. Alternate slides cut from primary tumor FFPE blocks were used for RNA-seq or H&E staining. RNA expression data and visual features extracted from H&E slides were then fed into NEXt. IHC staining for lineage specific immune markers (CD20, CD4, CD8, CD68, CD56) was used by a pathologist to establish immune infiltration proportions.

Solid tumors are commonly infiltrated by adaptive and innate immune cells, including T and B lymphocytes, natural killer (NK) cells, and macrophages (MACs).^{7,9} In the prevailing model, distinct effector cells in the tumor-immune microenvironment cooperate to present, recognize, and respond to tumor-specific antigens. However, several roadblocks exist for routine, accurate, and widespread pathological reporting of the immune infiltrate in tumor biopsies. Visual assessment after immunohistochemistry (IHC) staining for lineage specific markers remains the gold standard for evaluating immune cell infiltration in solid tumors. However, routine IHC assessment is not possible due to additional tissue sample requirements and the need for pathologist scoring. Alternatively, advances in genomic sequencing has facilitated implementation of RNA-sequencing (RNA-seq) in clinical medicine, but due to the inherent difficulty in deconvolving gene expression measurements into component immune cells, these approaches encounter significant ambiguity in reliably identifying correct immune proportions. Finally, emergent laboratory-based techniques, such as multiplex immunofluorescence, indexed flow cytometry, and single cell RNA-seq, require specialized labs and expertise, which limits widespread access.

We seek a middle ground by integrating coarse visual texture features from routine hematoxylin and eosin (H&E) staining of solid tumors used in cancer staging and diagnosis with bulk tumor RNA-seq to reduce ambiguity in predicting the immune infiltrate. In particular, this paper focuses on developing and applying a new framework, a neural network-based approach for integrating gene expression and visual texture features (NEXt) from solid tumor samples in a clinical laboratory setting (Fig. 1). We present implementations for predicting both the relative proportion of individual key effector immune cells and total fraction of the tumor immune infiltrate. Consequently, owing to the flexibility of our neural network-based approach, we are able to evaluate the integration of additional contextual features, such as estimates of the total fraction of immune infiltrate, to boost the prediction of immune cell-type proportions.

To test our model, we evaluated NEXt against current state-of-the-art methods for predicting the immune infiltrate as a proportion and benchmarked against expert pathologist review of IHC stained sections. Previous methods for predicting the immune infiltrate have either focused solely on RNA-based data or image-based data. Our approach is the first, to our knowledge, to utilize a multi-modal approach to refine RNA-based immune cell estimates by combining information from pathology imaging features.

2. Materials and Methods

2.1. *Data*

61 colorectal ($n = 14$), breast ($n = 15$), lung ($n = 17$) and pancreatic ($n = 15$) formalin-fixed paraffin-embedded (FFPE) solid tumor blocks were cut into alternating sections for RNA-seq, hematoxylin and eosin (H&E) staining, and immunohistochemistry (IHC) staining (Fig. 1A). Normalized read counts from RNA-seq for a specific panel of genes and visual texture features from H&E stained slides were generated and used as input for NEXT. Immune infiltrate predictions from NEXT were compared to pathologist expert review of IHC stained tumor sections using a panel of immune lineage markers (Fig. 1B).

2.1.1. *RNA extraction and sequencing*

Total nucleic acid was extracted from FFPE tumor tissue sections, macrodissected based on pathologist assessment of tumor cellularity, and proteinase K digested. Total nucleic acid was extracted with a Chemagic360 instrument using a source-specific magnetic bead protocol and stored at 4°C if less than 24 hours and -80°C if longer. RNA was purified from the total nucleic acid by DNase I digestion and magnetic bead purification. RNA was quantified by a Quant-iT picogreen dsDNA reagent Kit or Quant-iT Ribogreen RNA Kit (Life Technologies). Quality was confirmed using a LabChip GX Touch HT Genomic DNA Reagent Kit or LabChip RNA High HT Pico Sensitivity Reagent Kit (PerkinElmer).

The libraries were prepared using the KAPA RNA HyperPrep Kit. One hundred nanograms of RNA per tumor sample was fragmented with heat in the presence of magnesium to an average size of 200 base pairs. RNA underwent first strand cDNA synthesis using random primers, followed by combined second strand synthesis, A-tailing, adapter ligation, bead-based cleanup, and library amplification. After library preparation, samples were hybridized with the IDT xGEN Exome Research Panel. Target recovery was performed using Streptavidin-coated beads, followed by amplification using the KAPA HiFi Library Amplification Kit. The RNA libraries were sequenced to obtain an average of 90 million reads, minimum of 50 million reads, on an Illumina HiSeq 4000 System utilizing patterned flow cell technology.

After completion of sequencing, FASTQ files were uploaded to Amazon Web Services (AWS) which triggers the sequence analysis pipeline that uses the CRISP clinical RNA-seq pipeline¹⁰ orchestrated by the JANE workflow tool (Tempus Labs, Inc.). CRISP performs pre-alignment QC, read grooming, alignment, post-align QC, and gene level quantification. The gene level counts from CRISP are then converted to TPMs (transcripts per million) to normalize for gene length and library size.

2.1.2. *Visual texture feature extraction*

H&E stained slide images were tiled and downsampled, generating overlapping square tiles with 210x210 microns in tile size and 30 microns in shifting strip size. Image tiles were downsampled by 4 on each edge, as 1 micron equals 4 pixels in size. Statistical features for each tile were generated and converted into 196 feature vectors, consisting of intensity and texture features. Image intensity features included the mean, standard deviation, and sum, where

applicable, for the gray level; red, green, blue layer; H&E stain layers; optical density (od) 3 channels; hue; and saturation. Texture features included zernike moments¹¹ (0-24 moments), threshold adjacency analysis¹² values (statistics 0-53), local binary patterns¹³ (histogram bins 0-25), gray scale co-occurrence matrix¹⁴ and difference of Gaussian¹⁵ statistical measures. QuPath software¹⁶ was utilized for histology slide visualization, tissue detection and tiling. Scikit-image, scikit-learn and mahotas python libraries¹⁷ were used for image processing, feature generation and classification.

2.1.3. *Immunohistochemistry staining for lineage specific markers*

All FFPE slides were stained using the Leica Bond III automated IHC instrument and Leica reagents. The Leica antibody panel included: CD45 clone X16/99, CD4 clone 4B12, CD8 clone 4B11, CD20 clone L26, CD56 clone CD564, and CD68 clone 514H12. CD20 was used in a 1:200 dilution, but all other antibodies were purchased prediluted. Slides were deparaffinized using Dewax Solution. Heat induced epitope retrieval was used to reverse cross-linked proteins in the tissue by heating slides to 38 degrees Celsius and applying Epitope Retrieval Solution 1, a citrate-based solution with a pH of 6.0. The Bond Polymer Refine Detection kit was used for IHC staining and hematoxylin counterstaining. Slides were then dehydrated, mounted, and cover-slipped.

2.1.4. *Expert pathology review of histology slides*

The IHC and H&E stained slides were scored by a pathologist. The percent of each immune cell-type of interest (CD20+ B, CD4+ T, CD8+ T, CD68 MAC, CD56 NK cells) and total immune percentage (CD45) was determined by estimating the percent of cells that stained positive by IHC for the protein uniquely expressed by that cell-type. The pathologist was instructed to exclude staining of non-immune cells in their scoring. For instance, if 20% of all cells on a slide stained positively for CD20 B cells, but half of those positively staining cells were tumor cells, that sample would be scored as having 10% B cells. The percent tumor, stroma, and immune cells were estimated from evaluating the cell morphologies on their respective H&E slides. The relative abundance of the immune cell-types was determined by dividing the percent of the particular cell-type by the percent of total immune cells.

2.2. *NEXT architectures*

Neural networks can function as flexible and efficient learning models when integrating heterogeneous features, such as gene expression imaging features. The NEXT framework involves using a neural network-based architecture to integrate RNA-seq and imaging data. We used this framework in three separate architectures: NN-RNA, NN-RNA-image, and NN-Transfer (Fig. 2). Broadly, our framework was designed as a shallow neural network that consists of < 3 layers containing a set of neurons where each neuron is a weighted sum of the inputs in that layer. Non-linear activation functions are applied to the neurons to allow the model to find non-linear relationships between gene expression and imaging features. The output of a layer is then used as the input to the next layer. More specifically, given an input vector x , a

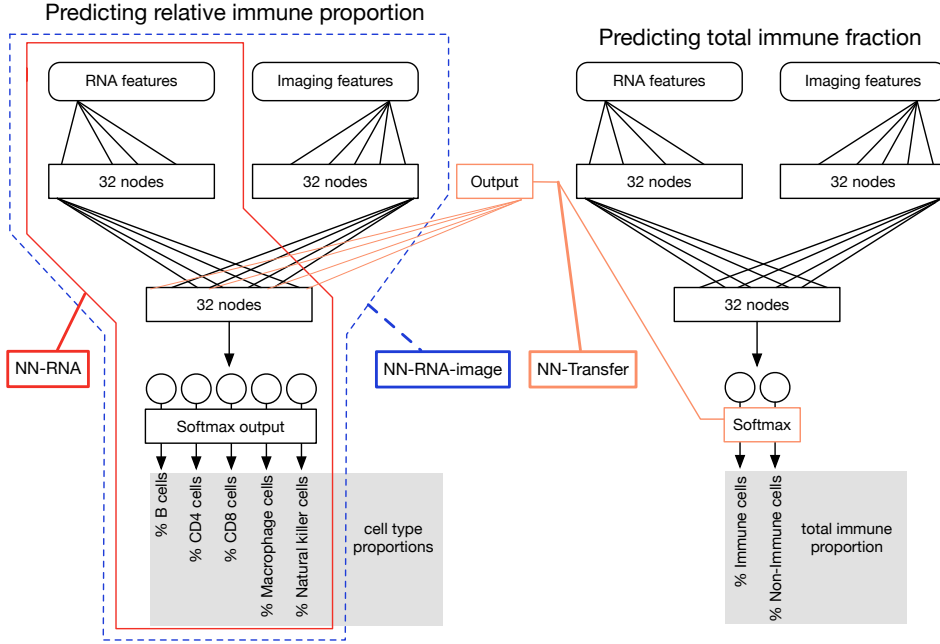


Fig. 2. NEXT architectures: NN-RNA (red), NN-RNA-image (blue), and NN-Transfer models (orange). The architecture takes in one or two inputs: RNA-seq gene expression alone (NN-RNA), or RNA-seq gene expression plus image features (NN-RNA-image). These inputs are passed into separate dense layers of 32 nodes in the first layer. The second layer contains a single dense layer of 32 nodes to integrate the information from the two sets of inputs. This layer is then fed into an output layer which uses the softmax activation to generate a probability distribution. These architectures can be used to predict relative immune cell-type abundances (left), or total fraction of tumor immune infiltrate (right). In the NN-Transfer model, we further boost the prediction of relative immune cell-type abundance through transfer learning by feeding the output of the total fraction of tumor immune infiltrate into the second layer of the model.

set of weights W , a bias term b , and an activation function ϕ , the output of the hidden layer, h , is calculated as:

$$h = \phi(Wx + b) \quad (1)$$

The neural network in this study was trained using both RNA-seq features and image features generated from image processing. The RNA-seq data was filtered using the LM22 gene list¹⁸ and the TPM values were log transformed (feature size = 547). The image features included the mean and skewness values of the intensity and texture features across all tiles in an image (feature size = 392). In the first layer of the network, each set of features was used as inputs to their own fully connected layer which used the rectified linear unit (ReLU) activation function.

$$\text{ReLU}(x) = \max\{0, x\} \quad (2)$$

The second layer concatenated outputs of the modularized dense layers to create an integrated set of features. The values from this second layer were then passed to an output layer which used the softmax function to predict the desired immune proportion. The softmax function squashes an n -dimensional vector of real valued numbers into a new n -dimensional vector

with values in the range $(0,1]$ and the sum of all the values is equal to one. More specifically, given a set of values for $Y = \{y_1, y_2, \dots, y_n\}$

$$\text{Softmax}(y_i|Y) = \frac{e^{y_i}}{\sum_j e^{y_j}} \quad (3)$$

Since our model was designed to predict a distribution, we trained it using the Kullback-Leibler divergence cost. The Kullback-Leibler divergence measures the divergence of a given probability distribution, Q , from a target probability distribution, P .

$$\text{KL}(P||Q) = \sum_i P(i) \log \frac{P(i)}{Q(i)} \quad (4)$$

To prevent over-fitting of our model, we applied an L2 regularization to the weights for every layer. This regularizes the model by diffusing the weight vectors so that the model uses all of its weights rather than relying on a subset of higher valued weights. We also sought to enforce a shallow neural network architecture by reducing layer sizes until performance degradation was observed. Our final cost function for training was

$$C = \sum_i y_i \log \frac{y_i}{\hat{y}_i} + \lambda \sum_L \|W^{(L)}\|_2 \quad (5)$$

Here y_i is the true value for the probability of the i th output, \hat{y}_i is the predicted probability for the i th output, λ is the L2 penalty coefficient, and $W^{(L)}$ are the weights for layer L .

The NN-RNA and NN-RNA-image architectures were trained to predict either the distribution of different immune cell-types in the sample or the total fraction of the tumor immune infiltrate. These models were trained using the ADAM optimizer for batch gradient descent with a learning rate of 0.005 and a λ value of 0.01. Models were trained and evaluated using leave-one-out cross validation. Specifically, for each left out example, we partitioned the other 60 samples into a training set of 40 and a validation set of 20. We then trained the model until the validation loss had not decreased within the last 5 epochs. We then predicted and reported the proportions of the single left out example.

After training the models, we evaluated if we could apply transfer learning by using one model to boost the other. For this, we used the outputs of the NN-Transfer model predicting the total fraction of the tumor immune infiltrate as additional inputs to the second layer of the NN-RNA-image model predicting the relative cell-type proportions. The NN-Transfer model was trained using the same methods and parameters described before.

3. Results

We tested the following four hypotheses. First, we tested whether NEXT could effectively learn and predict immune infiltration cell-type proportions from RNA-seq data (Section 3.1). Second, we tested whether integrating imaging features could further augment and improve infiltrate cell-type proportion prediction (Section 3.2). Third, we evaluated the flexibility of the NEXT architecture by predicting the total fraction of tumor immune infiltrate instead of the proportion of five key immune cell-types (Section 3.3). Finally, we tested the hypothesis that integrating estimates of the total fraction of immune infiltrate could yet further augment and improve prediction of the key immune cell-types (Section 3.4).

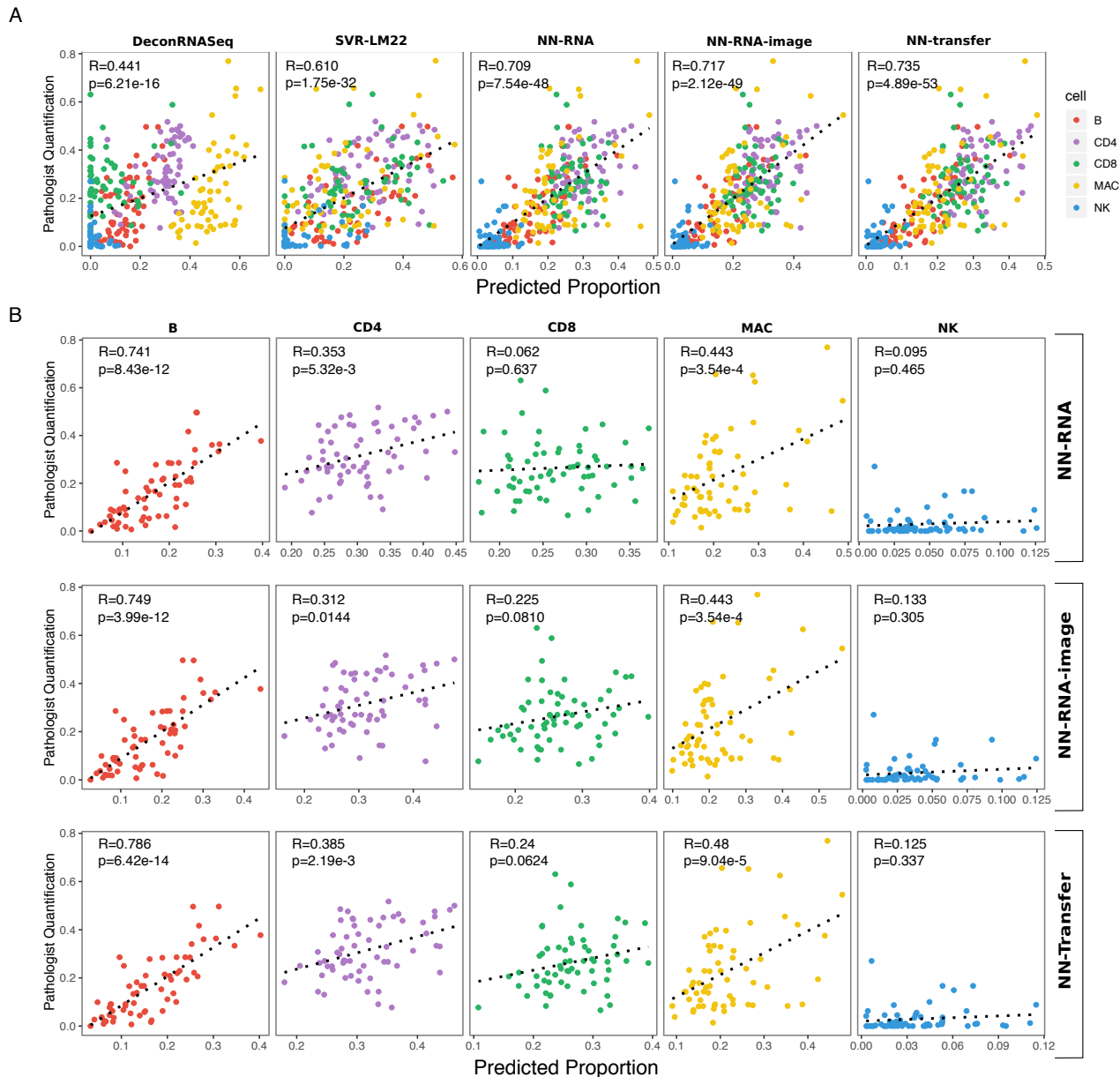


Fig. 3. Model performance benchmarking compared to expert pathologist assessment. (A) Predicted proportions of B, CD4 T, CD8 T, MAC, and NK cells of five models are shown in comparison to pathologist scoring of IHC lineage specific markers for 61 solid tumor samples. The sum of the proportions for all the cells for a particular sample will equal 1. The color of each point denotes the cell-type and the dotted line represents the linear regression line that best fits the data. The value of the Pearson correlation coefficient is shown in upper left corner of each plot. (B) The same data as (A) for the three neural network-based models (from top to bottom: NN-RNA, NN-RNA-image, NN-Transfer), but separated by immune cell-types.

3.1. *NEXT trained with RNA only (NN-RNA)*

Several groups have proposed methods for gene expression deconvolution using regression-based techniques. These include DeconRNASeq, which utilizes a non-negative linear regression

approach and CIBERSORT, which has demonstrated best-in-class performance for deconvolution using a support vector regression (SVR)-based approach.^{18,19} We sought to determine if NEXT could perform comparably to these algorithms when trained on RNA-seq data only (NN-RNA). Due to commercial restrictions, we independently implemented a support vector regression deconvolution algorithm using the LM22 matrix.¹⁸ Of the two regression-based techniques tested, we found that the SVR method performed better than DeconRNASeq, based on overall Pearson correlation.

To test the hypothesis that a neural network-based model (NN-RNA) could effectively learn immune cell proportions using RNA data only, we trained NEXT on the RNA-seq data using expert pathologist scoring of infiltration and evaluated performance using leave-one-out cross validation. The NN-RNA architecture was used to predict relative proportions for B, CD4 T, CD8 T, MACs, and NK cells. To establish a baseline against SVR, the RNA-seq data was filtered using the LM22 gene list and the TPM values were log transformed.

We found that NN-RNA performed better than SVR based on overall Pearson correlation ($R=0.709$; $p=7.54e-48$) (Fig. 3A). We attribute this improvement to two factors: (1) whereas SVR is a linear deconvolution method, NEXT can learn non-linear interactions between gene expression features; and (2) NEXT is trained and tested using RNA-seq data. While the authors of CIBERSORT indicate the SVR method with the LM22 matrix is amenable to RNA-seq data as well, we reason there is an advantage to using RNA-seq data for training when performing deconvolution on RNA-seq data. Overall, we find that NN-RNA effectively learns immune cell-type proportions and demonstrates better accuracies than current methods. Similar to SVR, NN-RNA performed best on B cells and worst on NK cells. This is likely due to B cells having a more distinct RNA profile, whereas NK cells likely share transcriptional similarities with CD8 T cells and comprise a smaller proportion of the immune infiltrate.²⁰

3.2. *NEXT trained with RNA and image features (NN-RNA-image)*

Information about infiltrating immune cells in histopathology slides is normally only accessible by overlaying additional multiplexed immunofluorescence or immunohistochemistry stains.²¹ We reason that embedded in microscopic H&E slides is latent information about the tumor-immune microenvironment, including the population structure and the underlying phenotypic states of the tumor and immune cells. Thus, we sought to test if integrating imaging features could further augment and improve the prediction of immune cell-type proportions.

To test this hypothesis, we obtained visual texture and intensity features from corresponding H&E images for each tumor sample. We utilized H&E image derived features due to the wide availability of H&E stained images used for cancer diagnosis and staging. To establish a baseline against NN-RNA, the RNA-seq data was filtered again using the LM22 gene list and the TPM values were log transformed. NN-RNA-image was trained to predict relative proportions for B, CD4 T, CD8 T, macrophage, and natural killer cells and was evaluated using leave-one-out cross validation.

NN-RNA-image boosted the prediction of immune cell-type proportions as evaluated by overall Pearson correlation ($R=0.717$; $p=2.12e-49$) (Fig. 3A). Of note, improvements were preferentially observed for CD8 T cells ($R=.225$; $p=0.081$) (Fig. 3B). These results suggest that

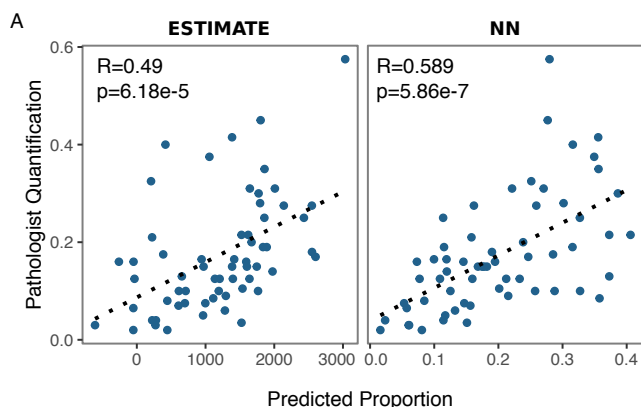


Fig. 4. Benchmarking of the total immune infiltrate fraction. Scatter plots illustrate pathologist counts compared to the immune score from ESTIMATE (left) and the predicted total fraction of immune infiltrate from NN-RNA-image (right).

integration of imaging features can function to improve immune infiltrate cell-type prediction.

3.3. *NEXT for predicting total tumor immune infiltration fraction*

Our choice of a generalizable neural network-based architecture for NN-RNA-image was deliberate as we hypothesized this could easily be adopted for other related but distinct tasks. We sought to evaluate the flexibility of NN-RNA-image in predicting the total fraction of immune infiltrate instead of the proportion of key immune cell-types. The total immune fraction framework seeks to predict the abundance of immune cells in the overall tumor microenvironment, in contrast to relative proportions of immune subsets in the total leukocyte population (Fig. 2). Here, a pathologist was instructed to assess immune cells (leukocytes) based on cell morphologies from patient H&E slides. We implemented a version of NN-RNA-image to predict two outputs, percent immune and non-immune fractions. We trained NN-RNA-image using RNA-seq data filtered using the LM22 gene set and imaging features. We evaluated performance using leave-one-out cross validation.

To benchmark our results, we analyzed samples with ESTIMATE, which is a tool for predicting tumor purity, and the presence of infiltrating stromal/immune cells in tumor tissues using gene expression data (Fig. 4).²² We found that a neural network-based model (NN-RNA-image) could be effectively adopted to learn the total immune infiltrate proportion. We found that our NN-RNA-image trained model performed better than ESTIMATE based on overall Pearson correlation. Taken together, NEXT provides a flexible framework for integrating RNA-seq and imaging features, and for predicting estimates of tumor immune infiltrate.

3.4. *NEXT augmentation with total immune infiltration fraction (NN-Transfer)*

Motivated by our previous results estimating the total fraction of immune infiltrate using both RNA-seq and imaging features, we sought to test the fourth hypothesis that integrating estimates of the total fraction of immune infiltrate could further augment and improve the prediction of infiltration cell-type proportions. We reasoned that including the total immune

and non-immune fraction may provide additional meaningful contextual features. Concomitant predictions of the total fraction of immune infiltrate were concatenated to the RNA-seq and imaging feature representations in the second layer of the network. Consistent with previous models, the RNA-seq data was filtered using the LM22 gene list and the TPM values were log transformed. We trained the NN-Transfer model using RNA-seq and imaging features and evaluated performance using leave-one-out cross validation.

We found increased accuracy in immune infiltrate prediction as evaluated by overall Pearson correlation ($R=0.735$; $p=4.89e-53$) (Fig. 3A, NN-Transfer). This increased accuracy was driven largely by increased correlations for specific immune cell-types, including B, CD4 T, and MACs (Fig. 3B). In sum, we demonstrate the flexibility and utility of our framework by transferring additional contextual features, suggesting that other relevant histological, molecular or clinical features can be readily integrated and used for more accurate immune infiltrate prediction.

4. Discussion

This study represents an important advancement in elaborating the tumor microenvironment by predicting the tumor immunological composition of individual patients. We present a multi-modal approach to estimating immune infiltration based on RNA-seq gene expression data and histopathology imaging features. We demonstrate the NEXT framework is efficient and flexible, allowing investigators to integrate pre-existing, routine clinical H&E stained slides with RNA-seq data (Fig. 1 and 2). We also demonstrate increased accuracy in predicting the abundance of key immune cell subtypes in solid tumors when compared to expert pathologist assessment of IHC (Fig. 3 and 4).

To our knowledge, this is the first report using multiple laboratory-based modalities to predict immune infiltration proportions in tumor samples and using gold standard expert pathologist reviewed IHC samples. Our particular focus on developing a generalizable and flexible framework for clinical RNA-seq and imaging data holds the potential for substantial clinical impact, including broadening widespread pathological reporting of the immune infiltrate in tumor biopsies and ultimately guiding patient treatment decisions.

We anticipate further research to fully evaluate these types of models in real-world clinical settings, and across a larger distribution and spectrum of cancer types. We note that our framework is amenable to larger datasets because it allows for larger or more layers to increase learning capacity. Larger datasets would also allow for learning unsupervised input features. Currently, our model incorporates supervised guided features of the human transcriptome and imaging data, but larger datasets can enable us to learn unsupervised H&E image features, such as through an auto-encoder, which may lead to performance boosts. Furthermore, our current model treats each cell type independently, but in some cases, the relative and absolute abundance of certain cell types may be correlated. Future work can also exploit the correlative structure of immune infiltration.

Additionally, as new routine and widespread laboratory-based techniques become adopted, our framework provides a principled approach for integrating relevant molecular and clinical features to further improve model performance. As we demonstrated in the NN-Transfer

model, the addition of other contextual information to the model can lead to better overall prediction accuracy. Other assays, such as DNA sequencing, radiological imaging, methylation profiling, immunofluorescence or other histological staining techniques, flow or mass cytometry, can be used to generate distinct features that can be integrated with the RNA and image components of the model in a similar fashion to NN-Transfer.

Finally, we note that NEXTE can also be used to train a model for predicting any arbitrary mixture of cells with known proportions. For instance, instead of immune cell subtypes or total immune fraction, the approach can be adjusted to estimate the relative proportion of tumor and endothelial cells, which would provide information about how much vascularization is present in a tumor. The utility of these models is also not limited to cancer samples. Inferring the relative and absolute proportions of different cell types in complex mixtures has value in many other disease areas, like lupus and rheumatoid arthritis, and is also a useful tool in basic science research.

Acknowledgments

The authors acknowledge and thank Dr. Alexandria Bobe for critical review, suggestions, and discussion. In addition, the authors thank Dr. Jason Perera, Dr. Alan Chang, Dr. Nike Beaubier, Dr. Tim Taxter, Dr. Stephen Yip and Ms. Erin McCarthy for immuno-oncology discussions, assistance with pathology review, immunohistochemistry services, tumor sample acquisitions, RNA-sequencing, digital imaging, and assistance with data retrieval.

References

1. Rizvi, N. A., Hellmann, M. D., Snyder, A., Kvistborg, P., Makarov, V., Havel, J. J., Lee, W., Yuan, J., Wong, P., Ho, T. S., Miller, M. L., Rekhman, N., Moreira, A. L., Ibrahim, F., Bruggeman, C., Gasmir, B., Zappasodi, R., Maeda, Y., Sander, C., Garon, E. B., Merghoub, T., Wolchok, J. D., Schumacher, T. N., and Chan, T. A. *Science (New York, N.Y.)* **348**(6230), 124–8 apr (2015).
2. Rooney, M. S., Shukla, S. A., Wu, C. J., Getz, G., and Hacohen, N. *Cell* **160**(1-2), 48–61 jan (2015).
3. Li, B., Severson, E., Pignon, J.-C., Zhao, H., Li, T., Novak, J., Jiang, P., Shen, H., Aster, J. C., Rodig, S., Signoretti, S., Liu, J. S., and Liu, X. S. *Genome biology* **17**(1), 174 dec (2016).
4. Herbst, R. S., Soria, J.-C., Kowanzetz, M., Fine, G. D., Hamid, O., Gordon, M. S., Sosman, J. A., McDermott, D. F., Powderly, J. D., Gettinger, S. N., Kohrt, H. E. K., Horn, L., Lawrence, D. P., Rost, S., Leabman, M., Xiao, Y., Mokatzin, A., Koeppen, H., Hegde, P. S., Mellman, I., Chen, D. S., and Hodi, F. S. *Nature* **515**(7528), 563–567 nov (2014).
5. Jenkins, R. W., Barbie, D. A., and Flaherty, K. T. *British Journal of Cancer* (118), 9–16 (2018).
6. Anitei, M.-G., Zeitoun, G., Mlecnik, B., Marliot, F., Haicheur, N., Todosi, A.-M., Kirilovsky, A., Lagorce, C., Bindea, G., Ferariu, D., Danciu, M., Bruneval, P., Scripcariu, V., Chevallier, J.-M., Zinzindohoue, F., Berger, A., Galon, J., and Pages, F. *Clinical Cancer Research* **20**(7), 1891–1899 apr (2014).
7. Alejandro Jiménez-Sánchez, A., Memon, D., Pourpe, S., Merghoub, T., Snyder, A., Miller Correspondence snyderca, M. L., Jiménez Sánchez, A., Veeraraghavan, H., Li, Y., Alberto Vargas, H., Gill, M. B., Park, K. J., Zivanovic, O., Konner, J., Ricca, J., Zamarin, D., Walther, T., Aghajanian, C., Wolchok, J. D., Sala, E., and Miller, M. L. *Cell* **170**, 927–938 (2017).
8. Chen, D. S. and Mellman, I. *Nature* **541**(7637), 321–330 jan (2017).

9. Woo, S. R., Corrales, L., and Gajewski, T. F. *Annual Review of Immunology* **33**(1), 445–474 mar (2015).
10. Robinson, D. R., Wu, Y.-M., Lonigro, R. J., Vats, P., Cobain, E., Everett, J., Cao, X., Rabban, E., Kumar-Sinha, C., Raymond, V., Schuetze, S., Alva, A., Siddiqui, J., Chugh, R., Worden, F., Zalupski, M. M., Innis, J., Mody, R. J., Tomlins, S. A., Lucas, D., Baker, L. H., Ramnath, N., Schott, A. F., Hayes, D. F., Vijai, J., Offit, K., Stoffel, E. M., Roberts, J. S., Smith, D. C., Kunju, L. P., Talpaz, M., Cieslik, M., and Chinnaiyan, A. M. *Nature* **548**(7667), 297–303 (2017).
11. Khotanzad, A. and Hong, Y. H. *IEEE Transactions on Pattern Analysis and Machine Intelligence* **12**(5), 489–497 May (1990).
12. Hamilton, N. A., Pantelic, R. S., Hanson, K., and Teasdale, R. D. *BMC Bioinformatics* **8**(1), 110 Mar (2007).
13. Harwood, D., Ojala, T., Pietikäinen, M., Kelman, S., and Davis, L. S. *Pattern Recognition Letters* **16**, 1–10 (1995).
14. Haralick, R. M., Shanmugam, K., and Dinstein, I. *IEEE Transactions on Systems, Man, and Cybernetics* **SMC-3**(6), 610–621 Nov (1973).
15. Lowe, D. G. *Int. J. Comput. Vision* **60**(2), 91–110 November (2004).
16. Bankhead, P., Loughrey, M. B., Fernández, J. A., Dombrowski, Y., McArt, D. G., Dunne, P. D., McQuaid, S., Gray, R. T., Murray, L. J., Coleman, H. G., James, J. A., Salto-Tellez, M., and Hamilton, P. W. *Scientific Reports* **7**(1), 16878 (2017).
17. Coelho, L. P. *CoRR* **abs/1211.4907** (2012).
18. Newman, A. M., Liu, C. L., Green, M. R., Gentles, A. J., Feng, W., Xu, Y., Hoang, C. D., Diehn, M., and Alizadeh, A. A. *Nature methods* **12**(5), 453–7 may (2015).
19. Gong, T. and Szustakowski, J. D. *Bioinformatics* **29**(8), 1083–1085 apr (2013).
20. Narni-Mancinelli, E., Vivier, E., and Kerdiles, Y. M. *International Immunology* **23**(7), 427–431 jul (2011).
21. Tsujikawa, T., Kumar, S., Borkar, R. N., Gray, J. W., Flint, P. W., and Coussens Correspondence, L. M. *CellReports* **19**, 203–217 (2017).
22. Yoshihara, K., Shahmoradgoli, M., Martínez, E., Vegesna, R., Kim, H., Torres-Garcia, W., Treviño, V., Shen, H., Laird, P. W., Levine, D. A., Carter, S. L., Getz, G., Stemke-Hale, K., Mills, G. B., and Verhaak, R. G. *Nature Communications* **4**(1), 2612 dec (2013).